Lecture 6: Introduction to spatially localized structures

Edgar Knobloch: notes by Srikanth Toppaladoddi and Cédric Beaume
with substantial editing by Edgar Knobloch

December 18, 2012

1 Introduction

Patterns are abundant in Nature. Some, for example, the stripe pattern on a zebra (or zebrafish!) arise for biological reasons, perhaps to serve as camouflage. However, essentially identical patterns are found in a variety of different physical and chemical systems. Figure 1 shows stripe patterns on a sand dune and in the atmosphere while Fig. 2 shows labyrinthine patterns in a ferrofluid system and on a pufferfish. The similarities between these patterns suggest the existence of general principles behind pattern formation that are independent of the detailed physics responsible for their presence. This is so for spatially localized patterns, too. In this lecture we shall look at spatially localized structures in a number of different physical systems in an attempt to illustrate the universal properties of such structures. We also introduce the Swift-Hohenberg equation that turns out to be very useful for studies of such structures, and show, using a multiple-scale analysis, how such an equation may arise in a fluid dynamical context, in this case as a description of gravity-capillary waves on the surface of an inviscid fluid.

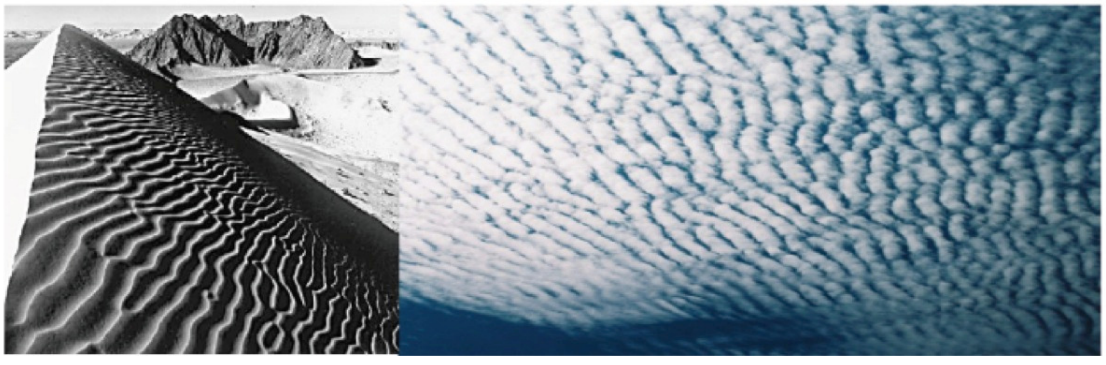

Figure 1: This image shows the stripe patterns on a sand dune (left), and in the cloud layer in the atmosphere (right). The patterns in these disparate systems bear strong resemblance.

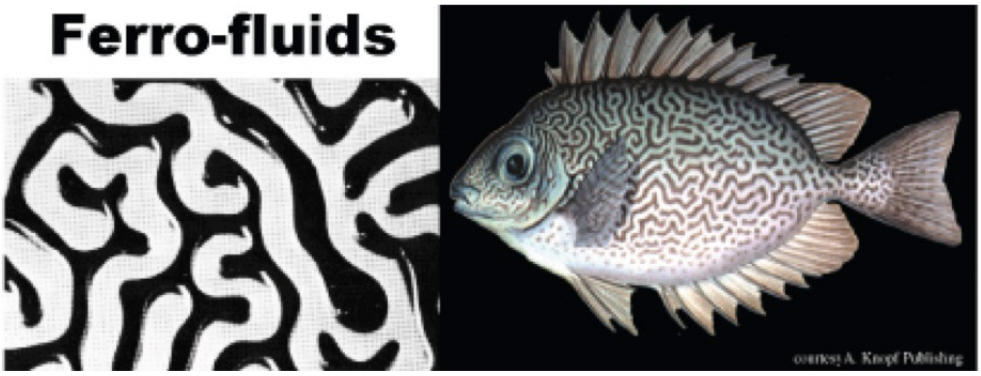

Figure 2: Labyrinthine patterns in a ferrofluid system (left), and on a pufferfish (right).

2 Localized structures in physical systems

There are many physical systems which show the presence of localized structures under appropriate conditions. In these lectures we shall be interested in localized structures in driven dissipative systems. Such structures are frequently referred to as *dissipative solitons* [22]. Structures of this type can be stationary or move. Here, we shall look at a few examples, and then introduce the Swift-Hohenberg equation that is a prototypical equation that exhibits structures of this type.

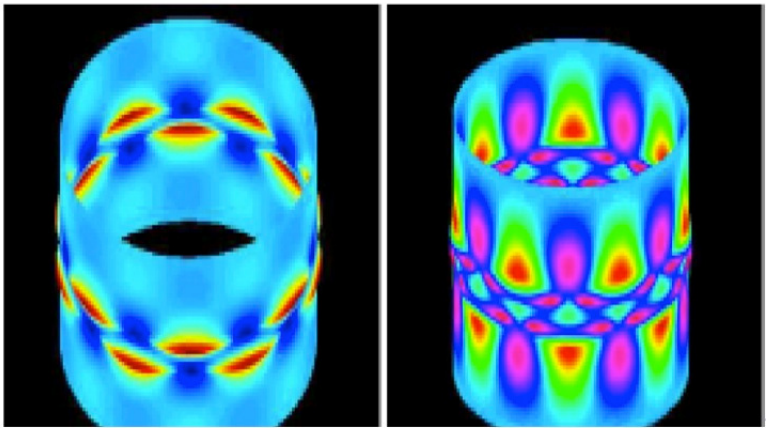

Figure 3: Displacement (left) and stress (right) patterns in a cylinder under axial loading. The displacement is the outward radial displacement measured from an unbuckled state. Both figures show a cellular pattern. From [15].

2.1 Cellular buckling in long structures

Hunt *et al.* [15] showed that when a tall structure, in their case a cylindrical shell, is loaded axially, the buckling of the structure may be confined to mid-section. The internal stress and displacement patterns formed are both cellular, and the number of these structures

increases with the magnitude of the load. Figure 3 shows the resulting cellular pattern, and in particular the localization of the displacement field for loads slightly larger than threshold. These buckled states may be stable, and although they are weaker than the unbuckled state, they are still able to support a load. However, when this load exceeds a critical value the structure collapses further, leading to a progression of buckled states consisting of more and more rows of cells.

The above results are best summarized in terms of a bifurcation diagram that tracks changes in the response of the system as a parameter changes. The variation in the parameter must be quasi-static; in simulations the parameter value is fixed for the duration of the simulation. The final state may then be used as the initial condition for a nearby parameter value. This process is laborious and numerical techniques have been developed to follow different states of the system without resorting to time-stepping. This approach offers considerable advantage in that unstable states can be followed as easily as stable states.

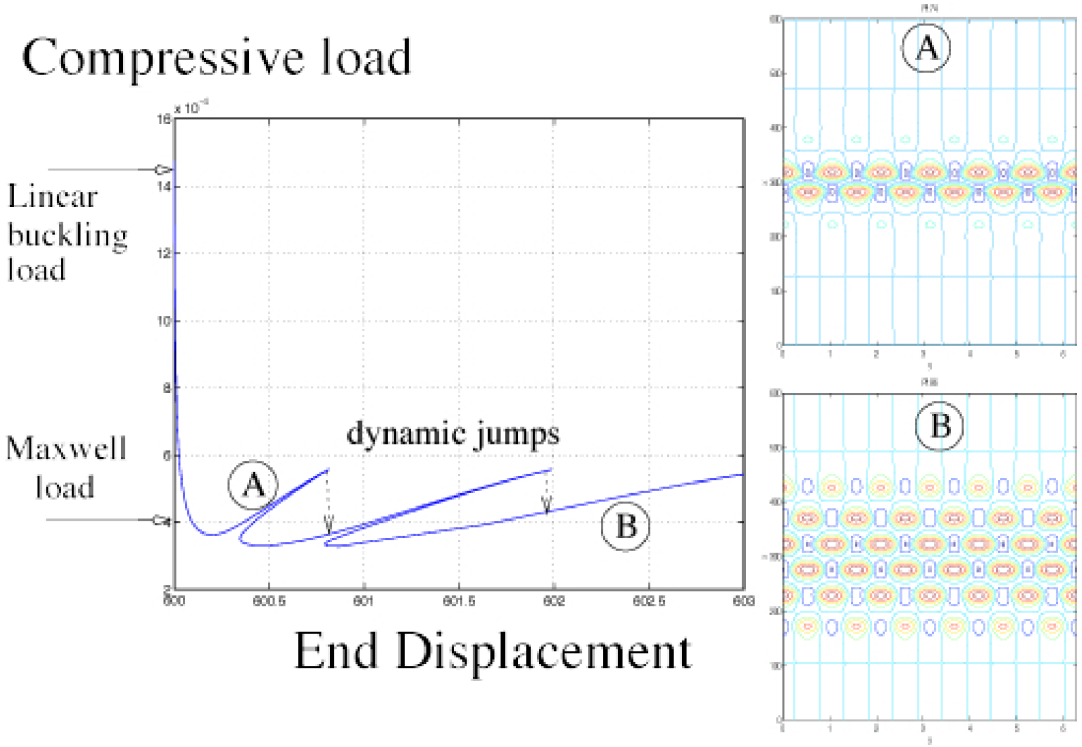

Figure 4: Bifurcation diagram for the buckling of an axially loaded cylinder. From [15].

Figure 4 shows the bifurcation diagram for the buckling problem. The diagram shows steady solutions of the system in terms of the end displacement as a function of the load parameter λ (plotted vertically). The unbuckled state loses stability at the linear buckling load. The bifurcation is strongly subcritical, meaning that for larger loads the buckling is catastrophic. For smaller λ, however, a variety of steady buckled states is present. These differ in the number of rows of cells generated, and these increase by two as the solution branch is followed. The states with positive slope are stable and can support increasing

load despite being buckled. When the load is increased too far a dynamic jump occurs to a state with an additional pair of rows etc. Thus there is a range of λ within which multiple stable solutions exist. The figure shows that these solutions are organized around a special value of the load parameter, called the Maxwell load. The significance of this parameter value will become apparent as the lectures proceed.

2.2 Solitons on the surface of a ferrofluid

A ferrofluid is a suspension of small magnetic dipoles. The free surface of this fluid undergoes a buckling instability, called the Rosensweig instability, when a uniform magnetic field of sufficiently large strength is applied in a direction normal to the surface [23]. This instability results in a hexagonal array of stationary peaks. Like the buckling of the cylindrical shell this instability is also strongly subcritical, leading to a broad region of magnetic field strengths for which the hexagonal pattern coexists with the flat surface. Within this region there is a subregion where multiple localized states can be created [23]. This can be done by bringing a bar magnet towards the surface, pulling out a peak, and removing the bar magnet. Remarkably, in this subregion the peak remains, and the process can therefore be repeated, pulling out more and more peaks. Figure 5 shows an example of a structure created in this way. Thus at every point in this subregion a number of different states, consisting of one, two, three or more peaks coexists with the flat and the hexagonal states, and all are simultaneously stable.

Figure 5: Two-dimensional localized structures on the surface of a ferrofluid. From [23].

Figure 6 shows the resulting bifurcation diagram. The diagram shows the surface energy as a function of the applied vertical magnetic field B. When B is increased from $B = 0$, the solution remains qualitatively unchanged until a threshold is reached at $B \approx 9$mT. At this value, a subcritical instability generates a hexagonal pattern of peaks. Since this is an experiment the small amplitude but unstable hexagons present for smaller B are not seen and the system jumps instead to a large amplitude hexagonal state. When B is decreased the hexagonal pattern persists until $B \approx 8$mT, where the peaks collapse and the flat interface is restored. The above process thus describes a hysteresis loop within which two stable states

coexist, the flat interface and the hexagonal pattern. The multi-peak states are present at $B = 8.91\text{mT}$, multi-peak states with $n = 1, 2, \ldots$ peaks were created by the process just described, leading to a large number of coexisting stable states at this parameter value.

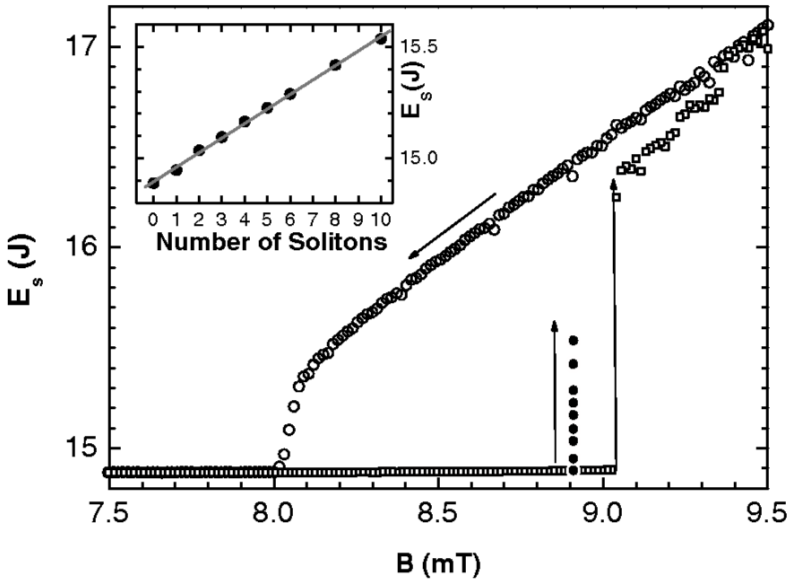

Figure 6: Bifurcation diagram for two-dimensional solitons on the surface of a ferrofluid showing the surface energy as a function of the imposed magnetic field B. Stable steady states with $n = 1, 2, \ldots$ peaks are present at $B = 8.9\text{mT}$. From [23].

2.3 Oscillons

Spatially localized oscillations called oscillons were found by Lioubashevski *et al.* [17] in experiments on a clay suspension subjected to vertical vibration. Figure 7 (left panel) shows an oscillon at several different times, while the right panels show different bound states of this type of oscillon. All states oscillate with twice the period of the forcing, i.e., all are subharmonic. Very similar behavior is present in vertically vibrated granular systems [26]. Figure 8 shows the interaction of two or more subharmonic oscillons created in this system.

Similar structures, called cavity solitons, are present in photonic systems [1]. Figure 9 shows how a cavity soliton is written and erased using a localized laser pulse.

2.4 Self-organized patterns in planar DC gas-discharge systems

Strumpel *et al.* [24] found that the discharge current in a DC-driven planar semiconductor gas discharge system is able to self-organize into a variety of nonlinear structures, including in some cases localized current filaments that interact in a manner similar to point vortices in fluid mechanics, i.e., via the Biot-Savart law. Figures 10 and 11 show some of these structures.

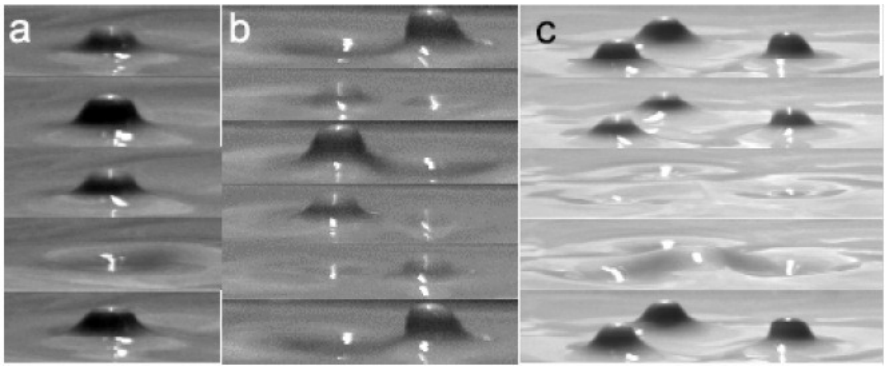

Figure 7: Oscillons on the surface of a clay suspension vibrated harmonically in the vertical direction. Figure (a) shows a single oscillon while (b) and (c) show different bound states of these oscillons. From [17].

2.5 Localized structures in fluid flows

There are many rich fluid dynamical systems where localized structures can be found. Some of them are briefly described here.

2.5.1 Convectons

Convectons, a term coined by Blanchflower [4], are stationary solutions of a convection problem consisting of convection rolls embedded in a background where heat is transported by conduction alone. Good examples of convectons have been observed in doubly diffusive convection. The first computation of convectons is due to Ghorayeb and Mojtabi [14] who studied a vertically extended rectangular cavity heated from one side in the presence of a parallel concentration gradient. When the concentration gradient is chosen appropriately the system possesses a conduction state for all values of a dimensionless number, the Grashof number Gr, that measures the thermal forcing of the system. However, this state loses stability at $Gr = Gr_c$ to a subcritical bifurcation, and for $Gr < Gr_c$ Ghorayeb and Mojtabi found the states shown in Fig. 12. Similar structures have also been found in magnetoconvection [4] and in binary fluid convection [2]. Figures 13 and 14 show examples of structures found in these systems. In all these examples the system forms convectons in response to a finite amplitude perturbation, and does so despite spatially uniform forcing. Each example also exhibits a multiplicity of different localized states under identical conditions.

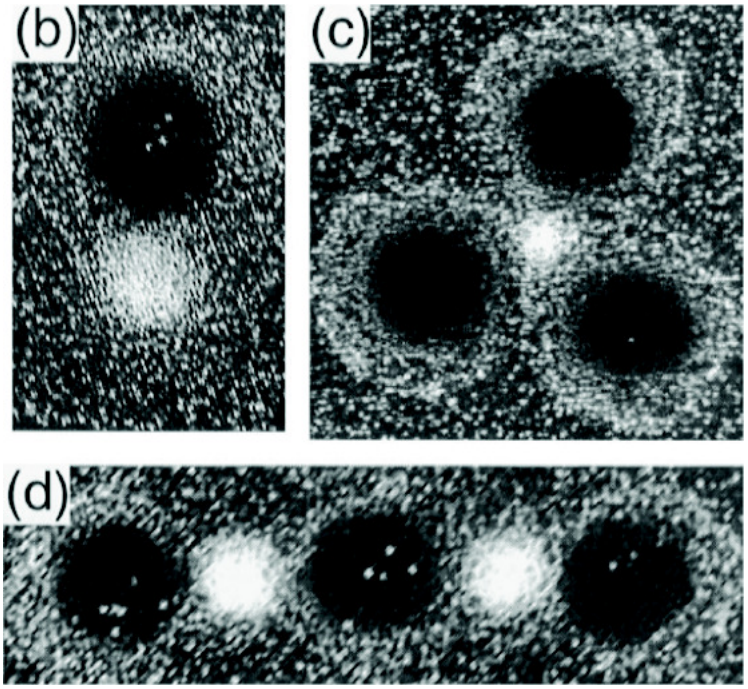

Figure 8: Oscillons in a granular system. From [26].

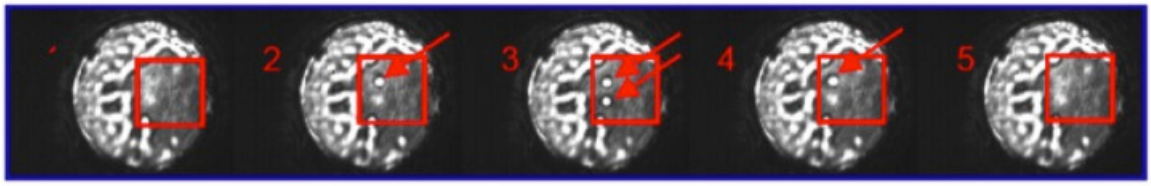

Figure 9: Writing and erasing of cavity solitons. From www.funfacs.org.

2.5.2 Shear flow

Shear flow also exhibits localization phenomena. Figure 15(a) shows a picture from an experiment by Gad-El-Hak *et al.* [12]. These authors studied the response of laminar flow over a stationary plate to a one-time perturbation generated by injecting additional fluid through a minute hole on the plate. The flow was visualized using fluorescent dye techniques. The tiny perturbation develops into a coherent structure whose Λ shape persists in time (Fig. 15(a)). Despite evident localization the structure is spatially and temporally complex.

Plane Couette flow provides perhaps the simplest example of a shear flow and is therefore of particular interest. This flow is generated by the motion of two parallel plates in opposite directions. The resulting linear velocity profile is stable for all plate velocities and a finite amplitude perturbation is needed to trigger persistent turbulence. The boundary in phase space between perturbations that decay to the laminar state and those that evolve into persistent turbulence is populated by unstable *edge states*. As shown in Fig. 15(b) some of these states may be localized. States of this type and the experimentally observed state

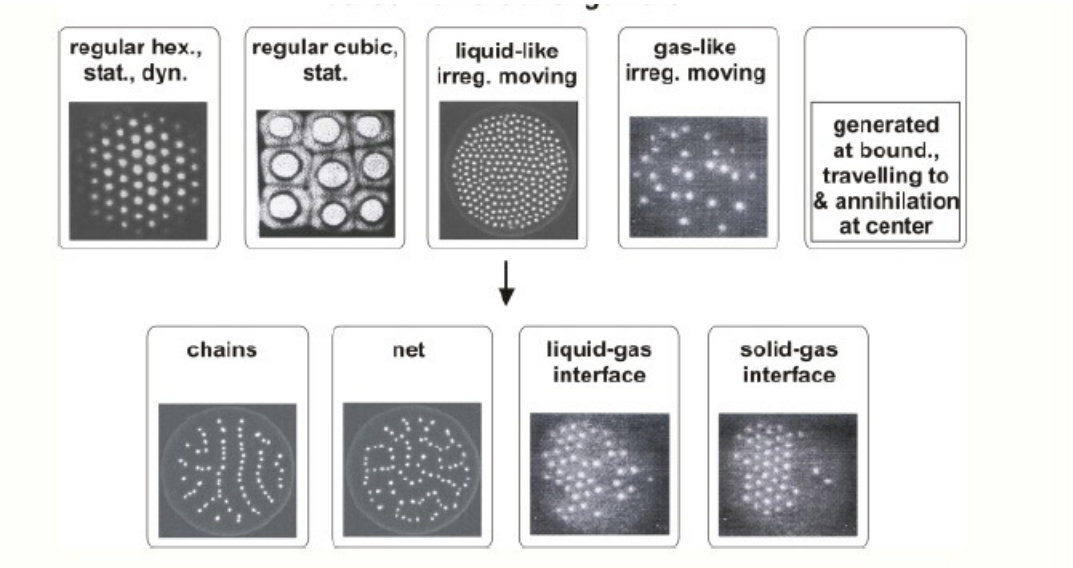

Figure 10: Different spatial patterns formed in a gas discharge system. From [21].

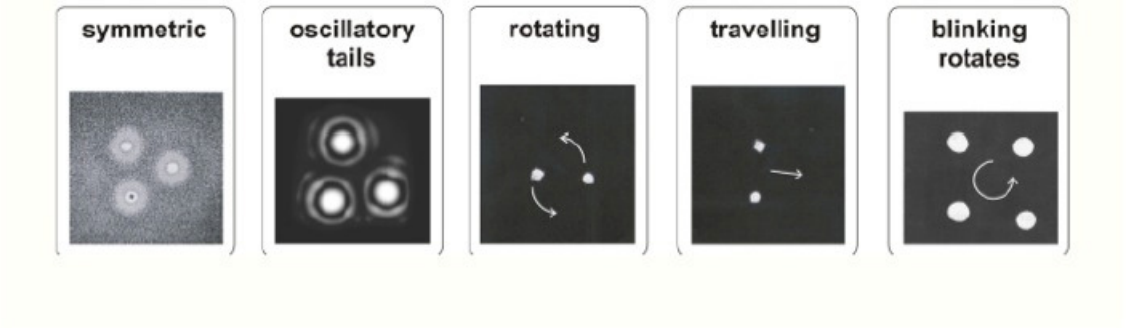

Figure 11: Point vortex-like structures found in a gas discharge system. From [21].

in Fig. 15(a) have some features in common suggesting that they may play a role in the transition to turbulence.

2.5.3 Defects

Defects in an otherwise periodic pattern can and should also be viewed as localized structures. Such defect states are most easily identified using demodulation techniques. Figure 1 shows several examples of defects in an otherwise periodic stripe pattern. Such defects typically move ("climb") and undergo a variety interactions. We shall not be discussing defects in these lectures.

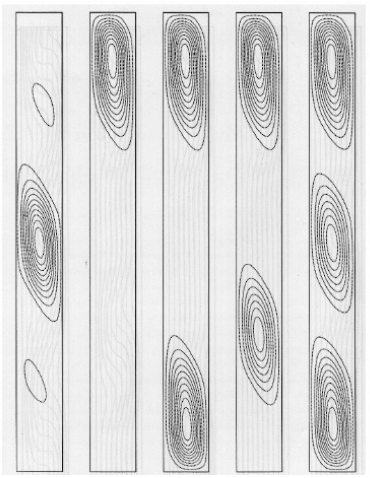

Figure 12: Different stable time-independent spatially localized structures in doubly diffusive convection in a rectangular cavity obtained for identical parameter values. The solutions are visualized using streamlines of the flow. From [14].

3 The Swift–Hohenberg equation

In the preceding section we have established a connection between the presence of spatially localized states and a subcritical bifurcation of a homogeneous state responsible for the coexistence of this state with a spatially periodic state. We have also seen that inside the resulting hysteresis loop one may find a large large multiplicity of coexisting localized states. We now turn to an explanation of this remarkable phenomenon. For this purpose we shall analyze in some detail a model problem, the Swift–Hohenberg equation [7, 8]. This equation was originally suggested as a description of pattern formation in Rayleigh–Bénard convection [19, 25] and it and its variants have led to substantial progress in our understanding of localized structures in driven dissipative systems in both one and two spatial dimensions [3, 18, 20]. However, its simplest realization is in the context of gravity-capillary waves on the surface of a liquid as described next.

3.1 Long gravity-capillary waves

Consider a two-dimensional fluid layer unbounded in x with $-H < y < \zeta(x,t)$, where H is the depth of the fluid and $\zeta(x,t)$ is the elevation of the surface relative to the undisturbed free surface at $y = 0$. The equations describing inviscid water waves read [27]:

$$\phi_{xx} + \phi_{yy} = 0 \qquad \text{in} \qquad -H < y < \zeta(x,t), \tag{1}$$

$$\phi_y = 0 \qquad \text{on} \qquad y = -H, \tag{2}$$

$$\zeta_t + \phi_x \zeta_x - \phi_y = 0 \qquad \text{on} \qquad y = \zeta(x,t), \tag{3}$$

$$\phi_t + \frac{1}{2}\left(\phi_x^2 + \phi_y^2\right) + g\zeta - \frac{\kappa \zeta_{xx}}{(1+\zeta_x^2)^{3/2}} = 0 \qquad \text{on} \qquad y = \zeta(x,t), \tag{4}$$

where $\phi(x,y,t)$ is the velocity potential, i.e., the velocity $(u,v) = (\phi_x, \phi_y)$. Equation (1) represents the incompressibility of the fluid, while Eq. (2) implies that the bottom boundary

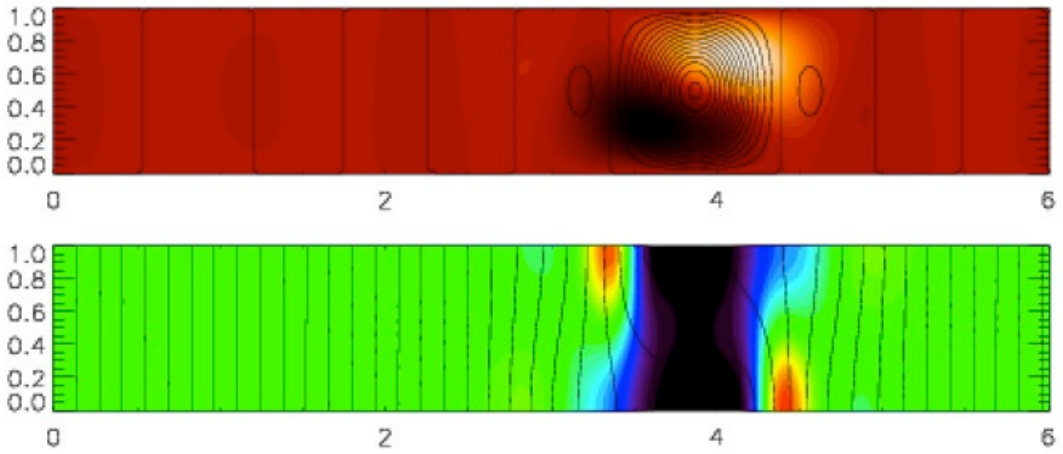

Figure 13: Time-independent spatially localized structure in magnetoconvection. Top panel shows the temperature fluctuation with superposed streamlines; the bottom panel shows contours of magnetic field strength with superposed magnetic field lines. From [5].

is impenetrable. Of the remaining equations Eq. (3) states that the interface moves with the local vertical velocity while Eq. (4) represents the Bernoulli's condition on the free surface. In this equation the last term represents the increase in pressure in the liquid due to surface deformation when the surface tension κ is nonzero.

3.2 Linear theory

The problem (1)–(4) has the trivial solution $\phi \equiv 0$, $\zeta \equiv 0$. We consider infinitesimal perturbations of the free surface of the form $\zeta = \zeta_0 \sin(kx - \omega t)$, where k is the perturbation wavenumber and ω is its frequency. This expression represents a periodic wave traveling to the right with phase speed $c = \omega/k$. Associated with this disturbance is a velocity disturbance given by $\phi = \phi_0(y)\cos(kx - \omega t)$, where the function $\phi_0(y)$ captures the decrease of the velocity with depth. With this Ansatz Eq. (1) yields

$$\phi_{0yy} - k^2 \phi_0 = 0. \tag{5}$$

The boundary condition (2) implies that $\phi_{0y} = 0$ at $y = -H$ and hence that

$$\phi_0 = A \cosh\left[k(y + H)\right], \tag{6}$$

where A is an arbitrary constant. The perturbed velocity potential then reads

$$\phi = A\cosh\left[k(y + H)\right] \cos(kx - \omega t). \tag{7}$$

Equation (3), linearized about $y = 0$, now yields

$$\zeta_0 \omega = -Ak \sinh(kH), \tag{8}$$

while Eq. (4) yields

$$-\omega A\cosh(kH) + g\zeta_0 + \kappa k^2 \zeta_0 = 0. \tag{9}$$

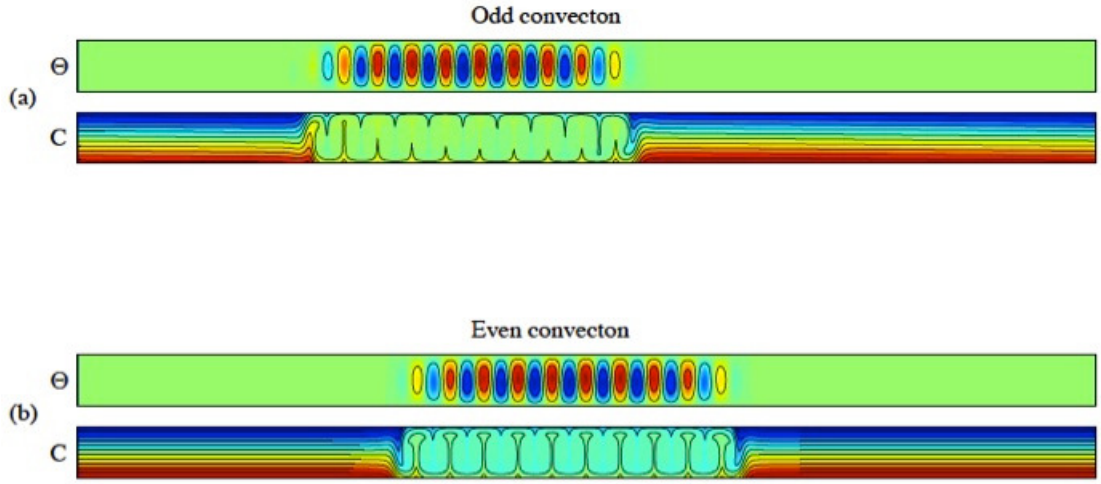

Figure 14: Coexisting stable odd and even convectons in binary fluid convection, shown in terms of the contours of the temperature fluctuation Θ relative to the conduction profile and of the concentration field C. From [2].

Elimination of the arbitrary amplitude A yields finally the dispersion relation for infinitesimal gravity-capillary waves:

$$\omega^2 = (g + \kappa k^2)k \tanh(kH). \tag{10}$$

We are interested in long waves, i.e., waves for which $kH \ll 1$. In this limit, the Taylor expansion of the hyperbolic tangent gives $\tanh(kH) = kH(1 - k^2H^2/3) + \mathcal{O}(k^5H^5)$ and the dispersion relation (10) becomes

$$\omega^2 = gk^2H + gk^4H^3(\mathrm{Bo} - 1/3) + \mathcal{O}(k^6), \tag{11}$$

where $\mathrm{Bo} \equiv \kappa/gH^2$ is the Bond number. Thus long waves are nondispersive at leading order but with a dispersive correction at higher order as described by the second term provided $\mathrm{Bo} \neq 1/3$. The special case $\mathrm{Bo} = 1/3$ is thus of particular interest, and in the following we study the weakly nonlinear regime near this special value of Bo.

3.3 Weakly nonlinear regime

Weakly nonlinear traveling waves are most easily found in the frame moving with the speed of the wave since in this reference frame the wave becomes stationary. We therefore set $\xi = x - ct$, and choose for c the long wave phase speed $c = \sqrt{gH}$. This will not in fact be the speed of the traveling wave since nonlinearity will modify its speed but it is a good first guess.

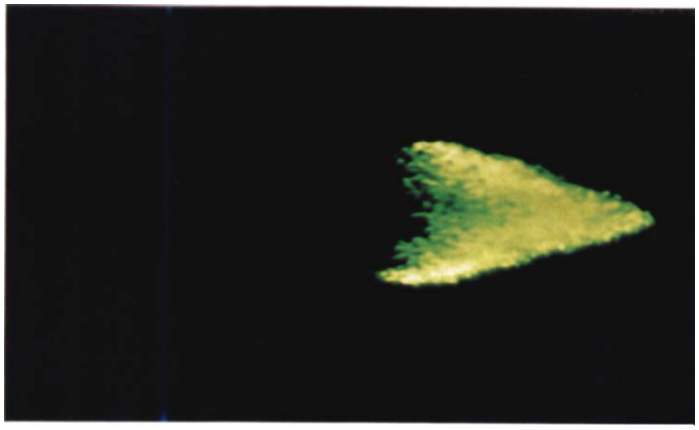

a)

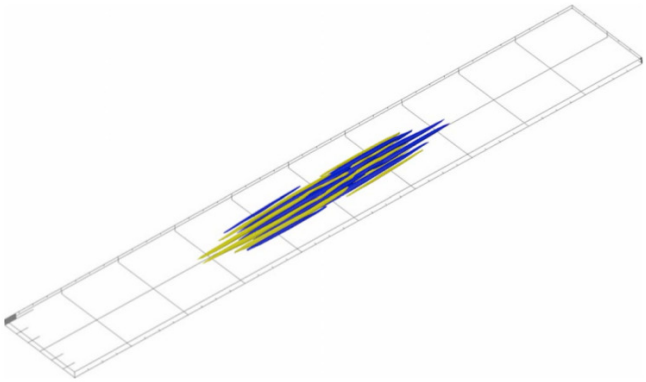

b)

Figure 15: (a) Two-dimensional spatially localized structure in boundary shear flow, viewed from above (from [12]). (b) Edge solution in plane Couette flow at $Re = 375$ in a $2\times30\times200$ domain. The structure is elongated in the streamwise direction, with yellow (blue) indicating positive (negative) streamwise velocity perturbation (from [10]).

In this frame Eqs. (1)–(4) become

$$\phi_{\xi\xi} + \phi_{yy} = 0 \qquad \text{in} \qquad -H < y < \zeta(\xi, t), \tag{12}$$

$$\phi_y = 0 \qquad \text{on} \qquad y = -H, \tag{13}$$

$$\zeta_t + c\zeta_\xi + \phi_\xi\zeta_\xi - \phi_y = 0 \qquad \text{on} \qquad y = \zeta(\xi, t), \tag{14}$$

$$\phi_t + c\phi_\xi + \frac{1}{2}\left(\phi_\xi^2 + \phi_y^2\right) + g\zeta - \frac{\kappa\zeta_{\xi\xi}}{(1+\zeta_\xi^2)^{3/2}} = 0 \qquad \text{on} \qquad y = \zeta(\xi, t). \tag{15}$$

Mass conservation requires that we impose the additional condition

$$\int_{-\infty}^{\infty} \zeta \, d\xi = 0 \tag{16}$$

on all our solutions.

We begin by defining a small parameter ϵ in terms of the departure of the Bond number away from its critical value, i.e., we write $\kappa = \kappa_0 + \epsilon^2\kappa_2$, where $\kappa_0 \equiv gH^2/3$ (corresponding to Bo $= 1/3$). Next we look for long waves with $\mathcal{O}(\epsilon)$ wavenumber, i.e., waves whose wavelength λ satisfies the relation $H/\lambda = \mathcal{O}(\epsilon)$. To do so, we introduce a large spatial scale $X = \epsilon\xi$ and a slow time scale $T = \epsilon^5 t$ that describes the evolution of the wave in the moving frame. The next step is harder because one needs to identify the scaling of the magnitudes of ϕ and ζ with ϵ that will lead to a balance between nonlinearity and the assumed weak dispersion. The correct choice is $\phi \to \epsilon^3\phi$ and $\zeta \to \epsilon^4\zeta$, yielding the scaled problem

$$\epsilon^2\phi_{XX} + \phi_{yy} = 0 \qquad \text{in} \qquad -H < y < \epsilon^4\zeta(X,T), \tag{17}$$

$$\phi_y = 0 \qquad \text{on} \qquad y = -H, \tag{18}$$

$$\epsilon^6\zeta_T + \epsilon^2 c\zeta_X + \epsilon^6\phi_X\zeta_X - \phi_y = 0 \qquad \text{on} \qquad y = \epsilon^4\zeta(X,T), \tag{19}$$

$$\epsilon^4\phi_T + c\phi_X + \epsilon^2\frac{1}{2}\left(\epsilon^2\phi_X^2 + \phi_y^2\right) + g\zeta - \epsilon^2(\kappa_0 + \epsilon^2\kappa_2)\zeta_{XX} = \mathcal{O}(\epsilon^{12}) \qquad \text{on} \qquad y = \epsilon^4\zeta(X,T). \tag{20}$$

We now expand ϕ and ζ in powers of ϵ^2: $\phi = \phi_0 + \epsilon^2\phi_2 + ...$ and $\zeta = \zeta_0 + \epsilon^2\zeta_2 + ...$ The leading order of Eqs. (17)–(18) indicates that $\phi_0 = f_0(X,T)$, where $f_0(X,T)$ is to be determined. At $\mathcal{O}(\epsilon^2)$, we obtain $\phi_{2yy} = -f_{0XX}$ with the boundary condition $\phi_{2y} = 0$ on $y = -H$. Thus

$$\phi_2 = -\frac{1}{2}(y+H)^2 f_{0XX} + f_2(X,T), \tag{21}$$

where $f_2(X,T)$ is unknown. Equations (19)–(20) on the boundary $y = \epsilon^4\zeta(X,T)$ give at leading order:

$$c\zeta_{0X} = -Hf_{0XX}, \tag{22}$$

$$cf_{0X} + g\zeta_0 = 0. \tag{23}$$

In view of the mass conservation condition (16), Eq. (22) can be integrated and gives $c\zeta_0 = -Hf_{0X}$ which, when combined with equation (23), gives the dispersion relation for long waves, viz., $c^2 = gH$.

At next order, Eq. (17) yields

$$\phi_{4yy} = -\phi_{2XX} = \frac{1}{2}(y+H)^2 f_{0XXXX} - f_{2XX}, \tag{24}$$

which can be integrated twice with respect to y:

$$\phi_4 = \frac{1}{24}(y+H)^4 f_{0XXXX} - \frac{1}{2}(y+H)^2 f_{2XX} + f_4(X,T), \tag{25}$$

where the boundary condition $\phi_{4y} = 0$ at $y = -H$ has been used to eliminate one constant of integration. The following order gives

$$\phi_{6yy} = -\phi_{4XX} = -\frac{1}{24}(y+H)^2 f_{2XXXX} - f_{4XX}, \tag{26}$$

leading to

$$\phi_{6y} = -\frac{1}{120}(y+H)^5 f_{0XXXXXX} + \frac{1}{6}(y+H)^3 f_{2XXXX} - (y+H) f_{4XX}. \tag{27}$$

These expressions are to be complemented with corresponding boundary conditions from Eqs. (19)–(20). At $\mathcal{O}(\epsilon^4)$, Eq. (19) reads:

$$c\zeta_{2X} = \phi_{4y} = \frac{1}{6}H^3 f_{0XXXX} - H f_{2XX}, \tag{28}$$

or

$$c\zeta_2 = \frac{1}{6}H^3 f_{0XXX} - H f_{2X}, \tag{29}$$

where we have again used the mass conservation relation (16) to fix the constant of integration. At $\mathcal{O}(\epsilon^2)$, Eq. (20) reads:

$$c\phi_{2X} + g\zeta_2 - \kappa_0 \zeta_{0XX} = 0, \tag{30}$$

or equivalently,

$$c\left(-\frac{1}{2}H^2 f_{0XXX} + f_{2X}\right) + g\zeta_2 + \frac{c\kappa_0}{g} f_{0XXX} = 0. \tag{31}$$

Notice that Eqs. (29) and (31) are identical provided $\kappa_0 = gH^2/3$. This fact confirms that we have scaled the linear terms correctly.

We proceed next to $\mathcal{O}(\epsilon^6)$ in Eq. (19):

$$\zeta_{0T} + c\zeta_{4X} + f_{0X}\zeta_{0X} = -\frac{1}{120}H^5 f_{0XXXXXX} + \frac{1}{6}H^3 f_{2XXXX} - H f_{4XX} - \zeta_0 f_{0XX}. \tag{32}$$

The last term in this equation arises from the ζ contribution to ϕ_{2y}. Equation (20) at $\mathcal{O}(\epsilon^4)$ yields:

$$\phi_{0T} + c\phi_{4X} + \frac{1}{2}f_{2X}^2 + g\zeta_4 - \kappa_0\zeta_{2XX} - \kappa_2\zeta_{0XX} = 0, \tag{33}$$

where ϕ_4 is to be evaluated at $y = 0$ using Eq. (25). Eliminating f_4 and ζ_4 from the resulting equations we obtain a solvability condition which can in turn be simplified by eliminating f_0 in favor of ζ_0. We obtain

$$\frac{2c}{H}\zeta_{0T} - \frac{3g}{H}\zeta_0\zeta_{0X} + \kappa_2\zeta_{0XXX} + \frac{1}{30}gH^4\zeta_{0XXXXX} = -\kappa_0\zeta_{2XXX} - \frac{1}{3}cH^2 f_{2XXXX}. \tag{34}$$

The right hand side of this equation can be evaluated in terms of ζ_0 with the help of Eq. (31) and the relation $\kappa_0 = gH^2/3$ leading finally to an evolution equation satisfied by ζ_0:

$$\frac{2c}{H}\zeta_T - \frac{3g}{H}\zeta\zeta_X + \kappa_2\zeta_{XXX} - \frac{1}{45}gH^4\zeta_{XXXXX} = 0. \tag{35}$$

In writing this equation we have dropped the subscript 0 on ζ_0. The resulting equation generalizes the Korteweg–de Vries equation by retaining higher order dispersion.

Solitary waves traveling to the right with speed V and without change of shape may now be obtained by writing $z \equiv X - VT$ to boost the reference frame by just the right amount

so that the nonlinear solution remains stationary. In this frame such a wave satisfies the ordinary differential equation

$$\frac{1}{45}gH^4\zeta'''' - \kappa_2\zeta'' + \frac{2cV}{H}\zeta + \frac{3g}{2H}\zeta^2 = 0 \tag{36}$$

obtained after one integration with respect to the variable z. Here the prime denotes a derivative with respect to z. The resulting equation is the simplest case of the Swift–Hohenberg equation, hereafter SH20, because it only includes a single nonlinearity of second order. Despite its simplicity this equation has a remarkably rich solution structure that includes a large number of solutions homoclinic to $\zeta = 0$, i.e., solitary waves [6, 11].

We remark that Eq. (36) is dissipative in *space* although the time-dependent problem from which it was derived is conservative, with an energy that is conserved in time.

4 The Korteweg–de Vries equation

The Korteweg–de Vries equation (named after [16]) can be derived from Eqs. (17)–(20) using a different scaling that is valid for all values of Bo that are not close to the critical value Bo = 1/3. This time we write $X = \epsilon\xi$, $T = \epsilon^3 t$, $\phi = \mathcal{O}(\epsilon)$, $\zeta = \mathcal{O}(\epsilon^2)$ and assume that $\kappa - \kappa_0 = \mathcal{O}(1)$. Thus, the small parameter ϵ is now defined by the ratio H/λ instead of being defined in terms of the Bond number. Proceeding as in the preceding section we obtain at second order

$$\zeta_T + \zeta\zeta_X + \zeta_{XXX} = 0, \tag{37}$$

where T and X have been rescaled to eliminate constants.

Waves of constant form can be found by writing $\xi \equiv X - VT$ and integrating the resulting equation twice. The Korteveg–de Vries equation (37) then takes the form of an equation for a particle in a potential,

$$\frac{1}{2}\zeta_\xi^2 + U(\zeta) = E, \tag{38}$$

where E is a constant and

$$U(\zeta) \equiv \zeta^3/6 - V\zeta^2/2. \tag{39}$$

The potential $U(\zeta)$ is represented in Fig. 16. Sinusoidal oscillations are present around the local minimum of the potential provided $E + 2V^2/3 \ll 1$. As E increases the oscillations become more and more nonlinear and their (spatial) period increases.[1] When $E = 0$ the solutions have infinite period, i.e., they are solitary waves. These form a one parameter family,

$$\zeta = a\,\mathrm{sech}^2\left[\frac{a}{2\sqrt{3}}\left(X - \sqrt{gH}t - \frac{a}{3}T\right)\right], \tag{40}$$

parametrized by the wave amplitude a. Thus all finite amplitude solitary waves travel faster than $\sqrt{gH}$ and larger solitons travel faster than smaller solitons. These solutions interact in a particle-like manner, i.e., they are in fact *true solitons* [13, 28]. This is a

[1] A second constant of integration must be included in $U(\zeta)$ in order to satisfy the mass conservation condition (16).

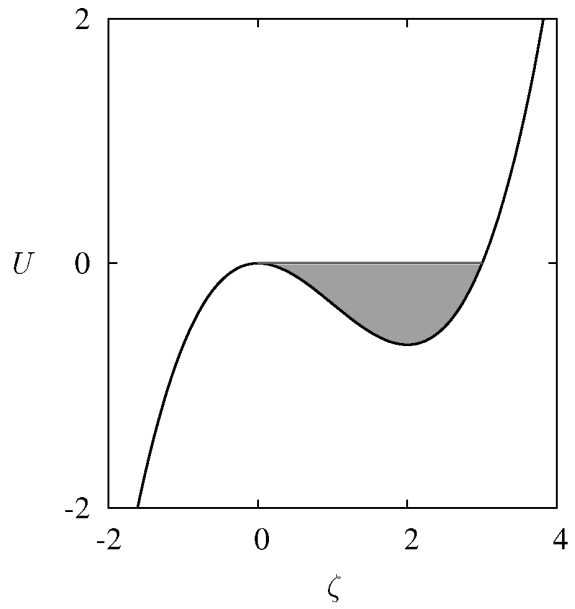

Figure 16: Potential $U(\zeta)$ in Eq. (39) when $V = 1$. The gray region indicates periodic solutions and the horizontal line delimitating this region at the top corresponds to a solitary wave.

consequence of complete integrability of the Korteweg–de Vries equation as an infinite-dimensional Hamiltonian system.

Soliton behavior of the solutions of the Korteweg–de Vries equation is shown in Fig. 17. The left figure shows one soliton drifting to the right without change of shape. The second figure shows the collision between two solitons with different amplitudes and hence different speeds. During their collision, they pass through each other and resume their course at the same speed after a slight delay.

5 Spatial eigenvalues and localization

In the Korteweg–de Vries problem one cannot tell the direction of propagation of the wave from the solution profile or even that the wave is traveling. This is a consequence of the invariance of the water wave problem under Galilean transformation, but this is not the case in driven dissipative systems. In such systems a solitary wave travels whenever it is not reflection symmetric. Generically, only reflection-symmetric states are stationary.

For solitary waves in driven dissipative systems, we therefore need to distinguish between stationary solitary waves and traveling ones. Suppose that $u_t = g(u, u_x, u_{xx}, ...)$, where g is real-valued and $g(\mathbf{0}) = 0$. Then, $g(u, u_x, u_{xx}, ...) = 0$ is a dynamical system in space, with phase space $(u, u_x, u_{xx}, \dots)$, and its solutions represent steady states. Of particular interest is the fixed point $u = 0$ in this phase space. This point represents a spatially homogeneous state and this state must have at least one unstable and one stable direction *in space* in order

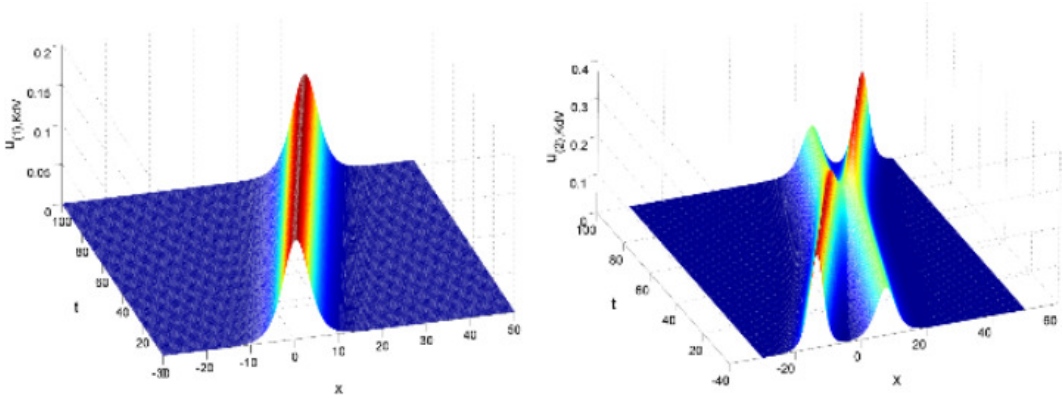

Figure 17: Left: spatio-temporal visualization of a Korteweg–de Vries soliton. Right: same type of visualization but for two different solitons. The soliton with larger amplitude travels faster as indicated by Eq. (40). After the collision the solitons continue their course with the same velocity but with a slight delay due to the collision. Courtesy L. Gelens.

that a solitary wave be present. Thus a necessary condition for the existence of solitary waves biasymptotic to the homogeneous state $u = 0$ is that $u = 0$ is a hyperbolic fixed point. To determine conditions for this to be so we must examine the spatial eigenvalues of $u = 0$. For this purpose we linearize $g(\mathbf{0}) = 0$ around $u = 0$,

$$g_u(\mathbf{0})u + g_{u_x}(\mathbf{0})u_x + g_{u_{xx}}(\mathbf{0})u_{xx} + ... = 0, \tag{41}$$

and look for solutions with $u = u_0 \exp \lambda x$. The spatial eigenvalues λ are thus given by

$$P(\lambda) = 0, \tag{42}$$

where P is real-valued so that $P(\lambda) = 0 \Rightarrow P(\bar{\lambda}) = 0$. If, in addition, the system is *spatially reversible*, meaning that it is invariant under spatial reflection, $x \to -x$, $u \to u$,[2] then $P(\lambda) = 0 \Rightarrow P(-\lambda) = 0$. Thus, if $u = 0$ has two negative real eigenvalues it also has two positive real eigenvalues. Likewise, if λ is a complex root of $P(\lambda) = 0$ then so are $-\lambda$ and $\pm\bar{\lambda}$ and the eigenvalues form a quartet in the complex plane. Thus, unless an eigenvalue has a zero real part, $u = 0$ has a two-dimensional unstable manifold W^u and a two-dimensional stable maniold W^s. If these manifolds intersect it is possible to find a trajectory that leaves $u = 0$ as x increases from $-\infty$ and returns to $u = 0$ as $x \to \infty$, i.e., a spatially localized solution. The likelihood of such an intersection is very much less when $u = 0$ has only one negative eigenvalue (and hence one positive eigenvalue), with the remaining eigenvalues on the imaginary axis.

It follows that in spatially reversible systems P is in fact a function of λ^2 and the simplest nontrivial case yields $P(\lambda) \equiv \lambda^4 + b\lambda^2 + a = 0$. Figure 18 depicts the location of the four eigenvalues of the spatial problem in the complex plane as a function of the parameters a and b. Below the curve $C_2 \cup C_3$, the eigenvalues lie on the axes, meaning that either their

[2]We remark that the Korteweg–de Vries equations (35) and (37) have a different type of spatial reversibility: $x \to -x$, $\zeta \to -\zeta$.

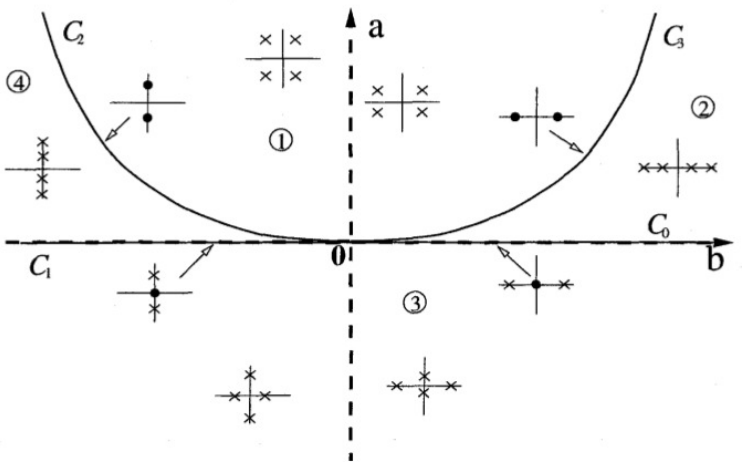

Figure 18: Roots of the equation $\lambda^4 + b\lambda^2 + a = 0$ in the (a, b) plane. From [9].

real part or their imaginary part is zero. Above this curve the eigenvalues form a complex quartet. We focus on the transition occurring at C_2. In the region labeled 4 in Fig. 18, all the eigenvalues lie on the imaginary axis, meaning the eigenmodes are purely oscillatory in space. As a or b increase the eigenvalues collide on the curve C_2 and move into the complex plane forming a quartet as anticipated above. This transition will provide a key to the appearance of spatially localized states as discussed in the next lecture.

In the Korteweg–de Vries case (37), the phase space of the equivalent particle-in-potential problem is two-dimensional and the fixed point $(u, u_x) = \mathbf{0}$ has a one-dimensional stable manifold W^s and a one-dimensional unstable manifold W^u. Consider the surface Σ representing $u_x(x = 0) = 0$ which is intersected by all spatially reversible solutions. Its dimension is $\dim(\Sigma) = 1$. The intersection $W^u \cap \Sigma$ is then a point and by reversibility this point is also on $W^s \cap \Sigma$. Thus the point $W^u \cap \Sigma$ lies on a homoclinic orbit to $(u, u_x) = \mathbf{0}$. This result also follows from "energy conservation" since both manifolds lie in the energy surface $E = 0$. Moreover, if $E \neq 0$ no homoclinic orbit is present implying that the homoclinic orbit is present at a single parameter value only.

The situation is quite different in the generalized Korteweg–de Vries equation such as Eq. (35) because this equation is of fifth order in space. Here the phase space of the equivalent dynamics problem is four-dimensional and in region 4 of Fig. 18 the fixed point $(u, u_x, u_{xx}, u_{xxx}) = \mathbf{0}$ has a two-dimensional stable and a two-dimensional unstable manifold. In four dimensions these manifolds will not intersect in general but we can find a large number of homoclinic orbits to $(u, u_x, u_{xx}, u_{xxx}) = \mathbf{0}$ by examining the vicinity of a *heteroclinic cycle* between this point and a symmetric periodic orbit Γ when such an orbit is present and is hyperbolic. This cycle consists of a heteroclinic connection from $\mathbf{0}$ to Γ followed by a heteroclinic connection from Γ back to $\mathbf{0}$. Note that if one can establish the presence of the first connection then the return connection follows using spatial reversibility. The periodic orbit plays a vitally important role in the generation of spatially localized states. The reason is that Γ has one zero eigenvalue (more correctly a Floquet multiplier equal to one) that is doubled by spatial reversibility. For Γ to be hyperbolic there must in

addition be one stable Floquet multiplier and one unstable Floquet multiplier. Under these conditions Γ has a three-dimensional center-stable manifold W^{cs} and a three-dimensional center-unstable manifold W^{cu}. Since an intersection between the two-dimensional unstable manifold W^u of $\mathbf{0}$ and the three-dimensional center-stable manifold W^{cs} of Γ is generic in four dimensions such an intersection cannot be perturbed away by making small changes to the parameter values (or indeed the equation). We call such intersections *structurally stable* and conclude, invoking spatial reversibility, that under these conditions the dynamical system $g = 0$ possesses a structurally stable heteroclinic cycle. Since such a heteroclinic cycle is associated with nearby homoclinic orbits (such orbits in fact accumulate on the cycle) it follows that near such a cycle one will find a plethora of homoclinics that persist over a finite parameter interval. We call such solitary waves *robust*.

In the next lecture we shall provide a concrete illustration of this abstract geometric argument. However, the argument suggests that the key to finding time-independent spatially localized states in reversible systems is provided by the presence of a heteroclinic connection $\mathbf{0} \to \Gamma$, i.e., of a *front* connecting a spatially homogeneous state to a spatially periodic state.

We mention that if spatial reversibility is absent then a heteroclinic cycle of the above type becomes of higher codimension and the situation becomes quite different. This is why the properties of traveling solitary waves differ substantially from those of stationary structures in spatially reversible systems.

References

[1] T. Ackemann, W. J. Firth and G.-L. Oppo. Fundamentals and applications of spatial dissipative solitons in photonic devices. *Adv. Atomic, Molecular, and Optical Physics,* **57**, pp. 323–421, 2009.

[2] O. Batiste, E. Knobloch, A. Alonso and I. Mercader, Spatially localized binary-fluid convection. *J. Fluid Mech.,* **560**, pp. 149–158, 2006.

[3] M. Beck, J. Knobloch, D. J. B. Lloyd, B. Sandstede and T. Wagenknecht. Snakes, ladders and isolas of localized patterns. *SIAM J. Math. Anal.* **43**, pp. 936–972, 2009.

[4] S. Blanchflower. Magnetohydrodynamic convectons. *Phys. Lett. A,* **261**, pp. 74–81, 1999.

[5] S. M. Blanchflower. *Modelling Photospheric Magnetoconvection.* Ph.D. Thesis, University of Cambridge, 1999.

[6] B. Buffoni, A. R. Champneys and J. F. Toland. Bifurcation and coalescence of a plethora of homoclinic orbits for a Hamiltonian system. *J. Dyn. Diff. Eq.* **8**, pp. 221–279, 1996.

[7] J. Burke and E. Knobloch. Localized states in the generalized Swift–Hohenberg equation. *Phys. Rev. E* **73**, 056211, 2006.

[8] J. Burke and E. Knobloch. Snakes and ladders: Localized states in the Swift–Hohenberg equation. *Phys. Lett. A* **360**, pp. 681–688, 2007.

[9] A. R. Champneys. Homoclinic orbits in reversible systems and their applications in mechanics, fluids and optics. *Physica D* **112**, pp. 158–186, 1998.

[10] Y. Duguet, P. Schlatter and D. S. Henningson. Localized edge states in plane Couette flow. *Phys. Fluids* **21**, 111701, 2009.

[11] A. R. Champneys and J. F. Toland. Bifurcation of a plethora of multi-modal homoclinic orbits for autonomous Hamiltonian systems. *Nonlinearity* **6**, pp. 665–721, 1993.

[12] M. Gad-El-Hak, R. F. Blackwelderf and J. J. Riley. On the growth of turbulent regions in laminar boundary layers. *J. Fluid Mech.* **110**, pp. 73–95, 1981.

[13] C. S. Gardner, J. M. Greene, M. D. Kruskal and R. M. Miura. Method for solving the Korteweg–de Vries equation. *Phys. Rev. Lett.* **19**, pp. 1095–1097, 1967.

[14] K. Ghorayeb and A. Mojtabi. Double diffusive convection in a vertical rectangular cavity. *Phys. Fluids* **9**, pp. 2339–2348, 1997.

[15] G. W. Hunt, M. A. Peletier, A. R. Champneys, P. D. Woods, M. Ahmer Wadee, C. J. Budd and G. J. Lord. Cellular buckling in long structures. *Nonlinear Dynamics* **21**, pp. 3–29, 2000.

[16] D. J. Korteweg and G. de Vries. On the change of form of long waves advancing in a rectangular canal and on a new type of long stationary waves. *Phil. Mag.* **39**, pp. 422–443, 1895.

[17] O. Lioubashevski, Y. Hamiel, A. Agnon, Z. Reches and J. Fineberg. Oscillons and propagating solitary waves in a vertically vibrated colloidal suspension. *Phys. Rev. Lett.* **83**, pp. 3190–3193, 1999.

[18] D. J. B. Lloyd, B. Sandstede, D. Avitabile and A. R. Champneys. Localized hexagon patterns of the planar Swift–Hohenberg equation. *SIAM J. Appl. Dyn. Sys.* **7**, pp. 1049–1100, 2008.

[19] Y.-P. Ma and E. A. Spiegel. A diagrammatic derivation of (convective) pattern equations. *Physica D* **240**, pp. 150–165, 2011.

[20] S. McCalla and B. Sandstede. Snaking of radial solutions of the multi-dimensional Swift–Hohenberg equation: a numerical study. *Physica D* **239**, pp. 1581–1592, 2010.

[21] H.-G. Purwins. Dissipative solitons in physical systems (http://www.osti.gov/eprints/topicpages/documents/record/112/2448809.html).

[22] H.-G. Purwins, H. U. Bödeker and Sh. Amiranashvili. Dissipative solitons. *Adv. Phys.* **59**, pp. 485–701, 2010.

[23] R. Richter and I. V. Barashenkov. Two-dimensional solitons on the surface of magnetic fluids. *Phys. Rev. Lett.* **94**, 185403, 2005.

[24] C. Strumpel, Yu. A. Astrov and H.-G. Purwins. Nonlinear interaction of homogeneously oscillating domains in a planar gas discharge system. *Phys. Rev. E* **64**, pp. 4889–4897, 2000.

[25] J. Swift and P. C. Hohenberg. Hydrodynamic fluctuations at the convective instability. *Phys. Rev. A* **15**, pp. 319–328, 1977.

[26] P. B. Umbanhowar, F. Melo and H. L. Swinney. Localized excitations in a vertically vibrated granular layer. *Nature* **382**, pp. 793–796, 1996.

[27] G. B. Whitham. *Linear and Nonlinear Waves*. Wiley, 1974.

[28] N. J. Zabusky and M. D. Kruskal. Interaction of 'solitons' in a collisionless plasma and the recurrence of initial states. *Phys. Rev. Lett.* **15**, pp. 240–243, 1965.